Optimized surface-emitting photonic-crystal terahertz quantum cascade lasers with reduced resonator dimensions

Gregoire Sevin,[1] Daivid Fowler,[1] Gangyi Xu,[1] Francois H. Julien,[1] Raffaele Colombelli,[1,a)]
Suraj P. Khanna,[2] Edmund H. Linfield,[2] and A. Giles Davies[2]
[1]*Institut d'Electronique Fondamentale, Univ. Paris Sud, UMR8622 CNRS, 91405 Orsay, France*
[2]*School of Electronic and Electrical Engineering, University of Leeds, Leeds LS2 9JT, United Kingdom*

(Received 10 June 2010; accepted 25 August 2010; published online 27 September 2010)

Terahertz frequency photonic-crystal quantum cascade lasers allow directional and controllable surface emission while at the same time functioning efficiently well above liquid nitrogen temperature. Through an in-depth understanding of the mechanism underlying surface emission, we demonstrate optimized devices with significantly reduced absolute threshold currents. We are able to reduce the device surface area by more than a factor of two, while maintaining angularly narrow, single-lobed surface emission with a divergence of $\approx 10^\circ \times 10^\circ$. The devices emit at $\sim 2.8-2.9$ THz, with maximum operating temperatures in the range 80–150 K. © *2010 American Institute of Physics*. [doi:10.1063/1.3489941]

Terahertz (THz) frequency quantum cascade (QC) lasers have become an extremely promising semiconductor laser source for the 1.2–5 THz frequency range ($\lambda = 250-60$ μm).[1] Target applications include astronomy, biosensing/imaging and spectroscopy, *inter alia*. In this context, research is being focused not only on increasing the maximum operating temperature, T_{max},[2] but also on "beam-shaping"[3,4] since the extreme light confinement typical of THz resonators generally yields highly nondirectional emission patterns.[3] Possible solutions include the use of horn-antennas,[4] second and third-order distributed feedback gratings,[5,6] and photonic-crystal (PhC) structures.[7–9] The single frequency surface emission characteristics of PhC devices are particularly attractive, as they offer the prospect of implementation in arrays of high brilliance sources for Fourier-transform infrared spectroscopy.

We have shown in Ref. 7 that the operation of PhC THz QC lasers is critically dependent on the absorbing boundary conditions, which can be experimentally implemented at the edges of the PhC resonators using the highly absorbing, doped semiconductor top contact layers (*absorbing edges*). Furthermore, the resonator in-plane quality factor ($Q_{\parallel}$), and thus the performance of PhC THz QC lasers, can be enhanced by grading the hole-radius across the lattice.[10,11] Combining this technique with the introduction of a π phase-shift in the PhC structure leads to single-lobed surface emission.[12,13] For example, the devices demonstrated in Ref. 10 had 14 and 18 PhC periods, were 454 μm and 584 μm wide, respectively, and led to single-lobed surface emission with a divergence of just $\approx 12^\circ \times 8^\circ$.

In this paper, we show that we can reduce further the device surface area, by more than a factor of two, by implementing an optimized PhC resonator design. We are able to reduce the absolute threshold current, while maintaining highly directional emission. Furthermore, we demonstrate explicitly that the electromagnetic near-field in the central part of the device is not associated with the surface emission process, enabling this redundant region to be used for wire bonding, leading to a further size reduction.

The GaAs/AlGaAs QC laser structure (wafer L207) used in this work has an emission frequency of ≈ 2.7 THz. For details of the heterostructure growth and design, see Ref. 8. The device area in PhC QC lasers scales in proportion to the square of the number of PhC periods but the area required for wire bonding remains constant, as does the absorbing edge width. These constraints limit the extent to which the miniaturization of devices is possible. We designed and fabricated a series of small PhC THz QC lasers (12-, ten-, and eight-period, with device sizes 390 μm $\times$ 390 μm, 324 μm $\times$ 324 μm, and 260 μm $\times$ 260 μm, respectively). Three different bonding schemes [Figs. 1(a)–1(d)] were then tested. One obvious solution for miniaturization is to employ only one pad for wire bonding, as shown in Figs. 1(a) and 1(b). Figure 1(a), in fact, shows a 12-period PhC cavity, similar—although smaller and with only one bonding pad—to those developed in Ref. 10. However, a single bond-

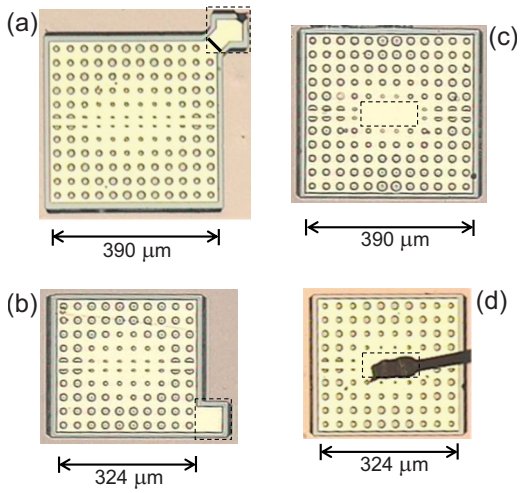

FIG. 1. (Color online) Images of typical devices (top view). The PhC period is 32.4 μm, the hole radius is graded to improve the in-plane Q-factor ($Q_{\parallel}$), and a π phase-shift is included. Areas assigned for wire-bonding are enclosed within dashed lines. (a) 12-period PhC with one bonding pad placed in the device corner, (b) ten-period PhC with one bonding pad placed on the device side, (c) 12-period PhC with central bonding pad, and (d) ten-period PhC with central bonding pad, and an actual wire-bond shown.

a)Electronic mail: raffaele.colombelli@u-psud.fr.

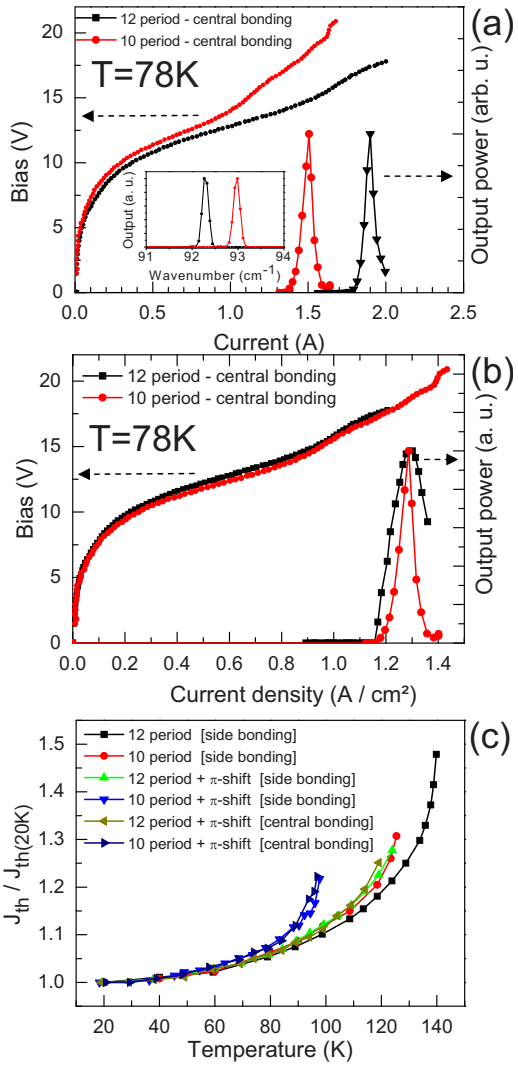

FIG. 2. (Color online) (a) *L-V-I* characteristics at a heat-sink temperature of 78 K for 12-period and ten-period PhC devices, with central wire-bonding [as shown in Figs. 1(c) and 1(d)]. Detection was achieved using a liquid-helium cooled bolometer. Devices were operated with 300 or 500 ns long pulses, at a repetition rate of 20–55 kHz. Inset: laser emission spectra of the two devices. (b) The data in (a) replotted in terms of the current *density* (*L-V-J*) characteristics. (c) Summary of the J_{th} dependence on heat-sink temperature for several devices with different dimensions (12-, ten-period), and different bonding schemes. J_{th} is normalized with respect to J_{th} at 20 K for each device. Results are also shown, for comparison, from PhC structures which do not have π phase shifts. Note: the *L-I*/*L-J* curves have been normalized and expressed in arbitrary units, as the relative output powers (which are in the milliwatts range) are significantly influenced by strong water absorption lines in this frequency range.

ing pad reduces the device symmetry. Far-field emission patterns measured from such devices are more angularly divergent than for two-pad devices (see later in the text), and this approach to size reduction also leads to strong secondary lobes in the far-field emission profile. In Figs. 1(c) and 1(d), a significant change was thus introduced into the design: the bonding area is now located in a metalized, nonpatterned central region ($\approx 65 \times 130$ μm^2) of the PhC. This modification simultaneously enables a reduction in overall surface area, easier wire bonding and an improvement of resonator symmetry.

Figure 2(a) shows typical light-voltage-current (*L-V-I*) characteristics of PhC devices with central bonding and a π phase shift. 12-period (390 $\mu m \times 390$ μm) and ten-period

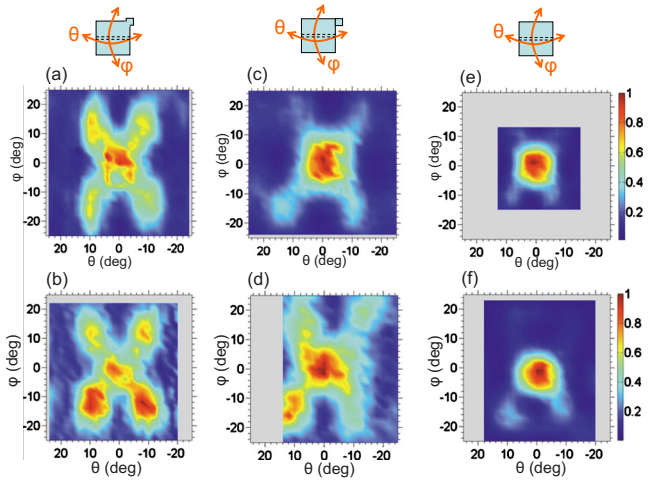

FIG. 3. (Color online) Far-field emission patterns of the PhC laser designs shown in Fig. 1, obtained by scanning a Golay cell detector at fixed distance from the sample, in steps of 2°. The top schematic diagrams define the angles of scanning and the device type. (a), (c), and (e) correspond to a 12-period PhC devices, while (b), (d), and (f) to ten-period devices.

(324 $\mu m \times 324$ μm) devices lased reliably, with or without a π phase-shift. Very small eight-period devices (260 $\mu m \times 260$ μm) did not, however, lase when bonded centrally. It should be noted that the lowest measured I_{th} is ≈ 1.35 A at 78 K, for the ten-period device. This is a significant improvement on previous, larger device designs[10] which had $I_{th} \approx 2.4$ A (3.7 A), for 14 (18)-period devices. All lasers exhibit single frequency emission [Fig. 2(a), inset], which confirms that the PhC resonator mode is correctly selected.

The absolute current threshold (I_{th}) scales well with the device surface area as demonstrated in Fig. 2(b) where the data in Fig. 2(a) is replotted in terms of current *density* for ten and 12 period PhCs. The *V-J* curves superpose almost perfectly, suggesting that current dispersion problems are insignificant. The *L-J* characteristics provide qualitative information on the relative device $Q_{\|}$, as J_{th} is inversely proportional to the total Q-factor. Assuming that the material Q-factor is the same for all structures, and the radiative Q-factor is negligible, a higher J_{th} corresponds to a lower $Q_{\|}$. In qualitative agreement with simulations, Fig. 2(b) shows that the J_{th} increases slightly when the size is reduced. This demonstrates that the lowest size for a THz PhC QC laser is limited by the $Q_{\|}$-factor, which decreases with reduction in size.

J_{th} is plotted as a function of heat-sink temperature in Fig. 2(c) for several devices with different dimensions. To simplify the comparison, all current densities are normalized with respect to their value at 20 K. The figure shows that T_{max} decreases with a reduction in the number of PhC periods, as well as with the introduction of a π phase-shift. However, all the devices operate well above 78 K.

Figure 3 presents the far-field patterns of the key PhC device designs. These were acquired by scanning a Golay cell on a sphere at constant radius from the laser surface. The top row of the figure defines the scanning angles and gives a graphical visualization of the device type—Figs. 3(a) and 3(b) thus correspond to the device designs illustrated in Fig. 1(a); Figs. 3(c) and 3(d) to the designs in Fig. 1(b); and Figs. 3(e) and 3(f) to the designs in Figs. 1(c) and 1(d). Importantly, the improved device architecture, with the central

bonding pad [Figs. 3(e) and 3(f)], avoids degradation of the far-field pattern with device size reduction. Almost ideal, single-lobed angularly-narrow emission patterns are obtained, in very good agreement with the numerical finite difference time domain (FDTD) far-field simulations of PhCs which include a central π-shift, as described in Refs. 8 and 10. Remarkably, in this improved design the emission pattern is affected only slightly by the device size. There is, therefore, no direct connection between the $Q_{\parallel}$ optimization/I_{th} reduction and the far field quality. In contrast, it is clear that the conventional ten-period and 12-period PhC devices exhibit far-fields with abnormally strong lateral lobes [Figs. 3(a)–3(d)], possibly a result of the presence of only one bonding pad.

The angular divergence of devices with a central bonding pad is narrow, with an approximate full width at half maximum of $10° \times 10°$. Directivity, D, can be used as figure of merit,[10,14] defined as $D = 10\log_{10}(2\pi I_{\text{peak}}/I_{\text{total}})$, where I_{peak} is the peak intensity (in watts per steradian) in the far-field, and I_{total} is the total emission power (in Watts) into half space. We obtain $D \approx 19-20$ dB for both the 12-period and the ten-period lasers with a central bonding pad. This value is slightly higher than that reported in Ref. 10 (16 dB) for larger devices but most importantly, it does not degrade with reduction in the surface area.

The counterintuitive result that the central bonding pad does not perturb the emission pattern can be explained by analyzing the near-field emission of the device. These devices operate on monopolar modes at the Γ-point of the PhC bandstructure. Monopolar Bloch modes of infinite PhC structures do not couple with the *continuum* of radiative modes, since the relative surface transverse fields are antisymmetric.[15,16] Surface emission is instead a consequence of the *finite* size of the devices. The Bloch mode is modulated by a spatially slowly-varying envelope function encompassing the whole structure, whose symmetry properties affect the device far-field. Since the envelope function is almost constant in the device center, this region does not contribute to surface emission.

This can be quantitatively illustrated by taking, for example, the y-component of the transverse, surface magnetic field H_y [Figs. 4(a) and 4(b)] and removing the components *outside* the light cone, which do not contribute to surface emission [Figs. 4(c) and 4(d)]. This operation yields only the contribution of the slow components, which are responsible for surface radiation. Calculations were undertaken using two-dimensional FDTD simulations—as in Ref. 8—followed by MATLAB postprocessing. The negligible contribution of the central part of the PhC resonator [Fig. 4(c)] explains why the device architecture presented in this paper works so efficiently. Removing the central holes does not change the distribution of the slow-components [Fig. 4(d)], and thus the central wire bonding can be applied without affecting the far-field distribution.

In summary, we have demonstrated optimized surface-emitting THz PhC QC lasers with both a reduced device surface area, and a reduced threshold current. The resulting emission patterns show a high directivity, which does not decrease with reduced device dimensions.

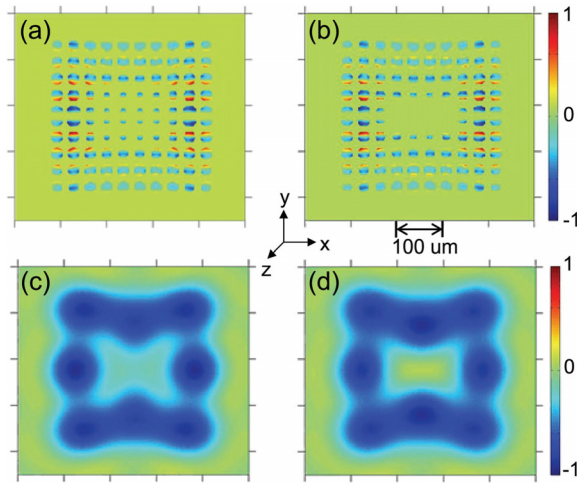

FIG. 4. (Color online) [(a) and (b)] Tangential y-component of the simulated magnetic field (H_y) in the PhC holes for a ten-period device with π phase-shift: (a) with central holes; (b) where the central holes have been removed. This field (and the corresponding H_x component) is used to calculate the far-field emission patterns shown in (c) and (d), where the tangential y-component of the simulated magnetic field (H_y) is shown after removal of the components outside the light cone. The central region does not contribute to surface emission.

The device fabrication has been performed at the Nano-Center CTU-IEF-Minerve, partially funded by the "Conseil Général de l'Essonne." This work was conducted as part of a EURYI scheme award. See www.esf.org/euryi. It was also supported by the French National Research Agency (Grant No. ANR-09-NANO-017 "Hi-Teq"), EPSRC EP/E048811 (U.K.), and the European Research Council Programmes "*NOTES*" and "*TOSCA*."

[1] R. Köhler, A. Tredicucci, H. E. Beere, E. H. Linfield, A. G. Davies, D. A. Ritchie, R. C. Iotti, and F. Rossi, Nature (London) **417**, 156 (2002).
[2] S. Kumar, Q. Hu, and J. L. Reno, Appl. Phys. Lett. **94**, 131105 (2009).
[3] P. Gellie, W. Maineult, A. Andronico, G. Leo, C. Sirtori, S. Barbieri, Y. Chassagneux, J. R. Coudevylle, R. Colombelli, S. P. Khanna, E. H. Linfield, and A. G. Davies, J. Appl. Phys. **104**, 124513 (2008).
[4] W. Maineult, P. Gellie, A. Andronico, P. Filloux, G. Leo, C. Sirtori, S. Barbieri, E. Peytavit, T. Akalin, J.-F. Lampin, H. E. Beere, and D. A. Ritchie, Appl. Phys. Lett. **93**, 183508 (2008).
[5] M. I. Amanti, M. Fischer, G. Scalari, M. Beck, and J. Faist, Nat. Photonics **3**, 586 (2009).
[6] S. Kumar, B. S. Williams, Q. Qin, A. W. M. Lee, and Q. Hu, Opt. Express **15**, 113 (2007).
[7] Y. Chassagneux, R. Colombelli, W. Maineult, S. Barbieri, H. E. Beere, D. A. Ritchie, S. P. Khanna, E. H. Linfield, and A. G. Davies, Nature (London) **457**, 174 (2009).
[8] Y. Chassagneux, R. Colombelli, W. Maineult, S. Barbieri, S. P. Khanna, E. H. Linfield, and A. G. Davies, Opt. Express **17**, 9491 (2009).
[9] G. Xu, Y. Chassagneux, R. Colombelli, G. Beaudoin, and I. Sagnes, Opt. Lett. **35**, 859 (2010).
[10] Y. Chassagneux, R. Colombelli, W. Maineult, S. Barbieri, S. P. Khanna, E. H. Linfield, and A. G. Davies, Appl. Phys. Lett. **96**, 031104 (2010).
[11] K. Srinivasan, P. E. Barclay, O. J. Painter, J. Chen, A. Y. Cho, and C. Gmachl, Appl. Phys. Lett. **83**, 1915 (2003).
[12] S. Li, G. Witjaksono, S. Macomber, and D. Botez, IEEE J. Sel. Top. Quantum Electron. **9**, 1153 (2003).
[13] E. Miyai and S. Noda, Appl. Phys. Lett. **86**, 111113 (2005).
[14] N. Yu, R. Blanchard, J. Fan, Q. Wang, C. Pflügl, L. Diehl, T. Edamura, M. Yamanishi, H. Kan, and F. Capasso, Opt. Express **16**, 19447 (2008).
[15] A. Taflove, *Computational Electrodynamics: The Finite-Difference Time-Domain Method* (Artech House, Norwood, MA, 1995).
[16] P. Viktorovitch, B. Ben Bakir, S. Boutami, J.-L. Leclercq, X. Letartre, P. Rojo-Romeo, C. Seassal, M. Zussy, L. Di Cioccio, and J.-M. Fedeli, Laser Photonics Rev. **4**, 401 (2010).